Engineering Structures 276 (2023) 115345

Contents lists available at ScienceDirect

Engineering Structures

journal homepage: www.elsevier.com/locate/engstruct

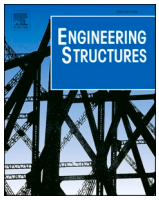

A machine-learning method for deriving state-dependent fragility curves of existing steel moment frames with masonry infills

Jing-Ren Wu *, Luigi Di Sarno

Dept. of Civil Eng. & Industrial Design University of Liverpool, L69 3GH Liverpool, UK

ARTICLE INFO

Keywords:
Neural networks
Existing steel frames
Masonry infills
Fragility curves

ABSTRACT

Seismic assessment of existing buildings is usually a building-specific task that relies on refined finite element models. Such a task may require considerable computational demand, especially when predicting the seismic fragility of existing buildings under the framework of performance-based earthquake engineering. However, the computational cost can be significantly reduced by replacing the finite element model with a well-trained machine learning-based model, for example, an artificial neural network model. This paper presents the application of feedforward neural networks to derive the state-dependent fragility curves of existing steel moment frames, taking into account the effects of masonry infills. The network models can be trained to predict explicitly whether a structure exceeds the target limit state based on representative intensity measures of ground motions, which is in nature a binary classification problem. The number of non-linear time-history analysis required to generate the training data for the network models tends to be significantly lower compared to the case of conventional incremental dynamic analysis, particularly when a great number of ground motions are adopted aiming at higher accuracy of the fragility curves.

1. Introduction

The evaluation of seismic vulnerability constitutes an essential part of seismic assessment of existing steel buildings. It is usually achieved by means of fragility analysis under the framework of performance-based earthquake engineering [1]. State-dependent fragility curves are a common way to illustrate the seismic vulnerability of structures in a probabilistic manner, which describe the probability of exceeding a specific limit state given the intensity of ground motions (GMs) [2]. Conventionally, the derivation of fragility curves, through either the incremental dynamic analysis (IDA) [3] or the multiple stripe analysis (MSA) [4], relies on performing a great number of nonlinear time-history analyses (NTHA) to obtain the structural response, thus is computationally expensive and time-consuming. However, the rapid development of machine learning techniques has provided strong tools to reduce significantly the computation cost and the time required to perform fragility analysis.

Machine learning (ML) refers to methodologies that can detect the hidden patterns behind data without being explicitly programmed in order to establish forecasting models and support decision making under uncertain conditions [5,6]. Currently the majority of ML algorithms can be categorised into two main groups, namely supervised learning and unsupervised learning. Supervised learning uses labelled training data to develop a predictive model that is able to map a set of input data to the output data, which is usually adopted to solve classification and regression problems. On the other hand, unsupervised learning uses data without clear target labels to infer the underlying structure behind a set of data, thus is usually selected for clustering and dimensionality reduction problems [8]. In the field of structural and earthquake engineering, the application of ML techniques has been widely demonstrated in literature to address problems such as structural design and modelling, and seismic assessment e.g., [7–13] among others.

In particular, many previous studies in literature have implemented ML models in the derivation of fragility curves for steel and reinforced-concrete moment frames to help minimise the computational demand. One of the fundamental applications of ML models in this regard is to predict the structural response based on representative intensity measures (IMs) of GMs and structural properties [14–16]. In this way, the output of ML models is usually directly the engineering demand parameter (EDP) chosen for the fragility curves other than the complete time-history of structural response. Alternatively, there are also attempts to use ML models to estimate the parameters governing the

* Corresponding author.
E-mail address: jingren.wu@liverpool.ac.uk (J.-R. Wu).

https://doi.org/10.1016/j.engstruct.2022.115345
Received 25 August 2022; Received in revised form 13 November 2022; Accepted 19 November 2022
Available online 2 December 2022

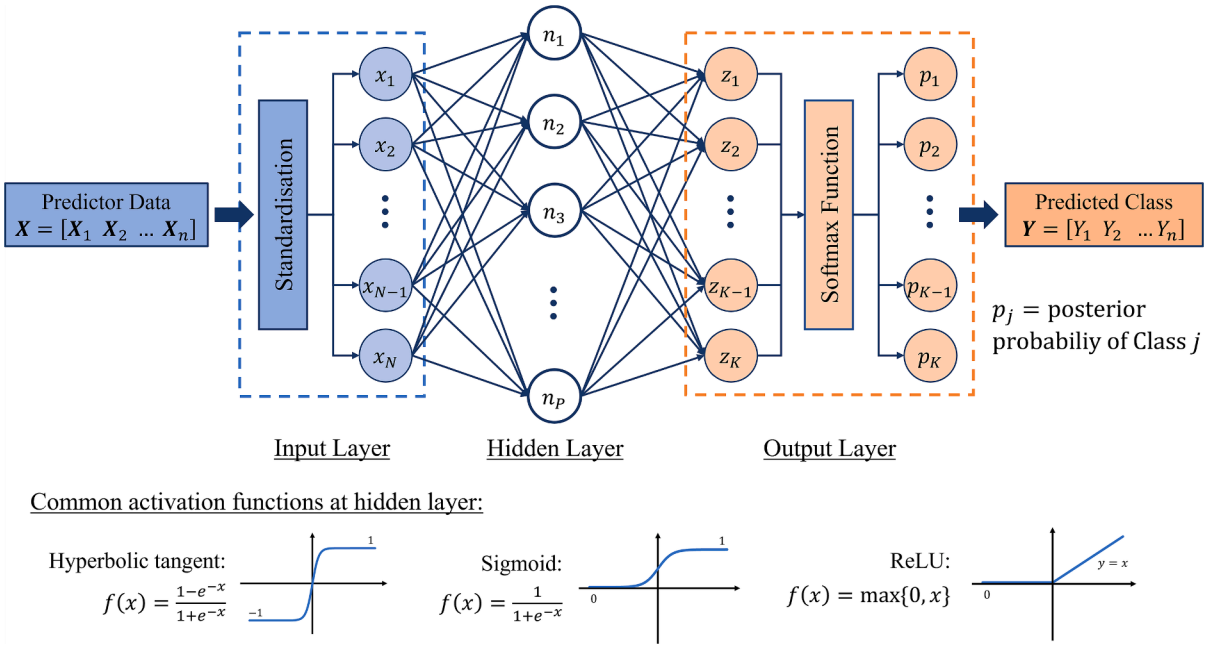

Fig. 1. The structure of a feedforward neural network model with single hidden layer.

fragility functions. e.g., [17–19], such as the median and dispersion of the collapse intensity, which eventually lead to the fragility curves in a more straightforward manner. In addition, there are also a few studies using classification models to estimate the damage state of structures, i.e. the whether a limit state has been exceeded, thus state-dependant fragility curves can be derived in a different approach [20,21].

Nonetheless, most of the previous studies have not yet considered the effects of infill walls on the response of framed structures, particularly in the case of assessing the vulnerability of existing steel moment frames. It has been reported in many previous studies e.g., [22–24] that the presence of infill walls can considerably increase the lateral stiffness and strength of existing steel moment frames, and improve the energy dissipation capacity under seismic loading. However, infill walls can also cause stress concentration at beam-column connections, leading to increased local seismic demands. Therefore, to adequately account for the effects of masonry infills, several modelling strategies of masonry infills have been developed in literature [22,25–27]. Among others, the single-strut model is one of the most popular modelling methods for infill walls, which represents the infill wall by two compression-only struts, one in each diagonal direction of the wall panel e.g., [28–30]. Such models are easy to implement and have been proved to be capable of accurately predicting the global structural response, which are usually sufficient for the derivation of fragility curves using inter-storey or roof drift as the EDP. The low computational demand of single-strut models also allows for fast generation of database for training the neural network models, leading to a promising approach for fast derivation of fragility curves.

Furthermore, the majority of previous research has focused on the use of regression models to predict the structural response, while only a few attempts have been made to the use of classification models. Considering that the main task in the derivation of fragility curves is for each GM to determine whether the structure is safe under the limit state being assessed, which is naturally a binary classification problem. Therefore, it can be beneficial to employ classification models in the derivation of fragility curves of existing steel moment frame, especially when the effects of infill are taken into account.

To this end, the aim of this paper is to present the use of neural network classification models to derive fragility curves of existing steel moment frames, taking into account the effects of masonry infills. Four case study buildings representing low- and mid-rise existing steel moment frames designed for low and high seismicity were selected to demonstrate the proposed method. Fragility curves were then obtained for all the case study buildings using the proposed method and compared with the results obtained from conventional IDA in order to assess the accuracy and efficiency of the proposed method.

2. Research significance

The present work investigates the capability of neural network classification models in the derivation of state-dependent fragility curves of masonry-infilled existing steel moment frames. In particular, the effects of masonry infills are accounted for by adopting the single-strut model in the modelling of infilled steel moment frames when generating the data for the fragility curves. As the infill walls often represent an essential source of the inelastic behaviour of existing steel moment frames, which causes increased difficulty in obtaining a reliable ML model, it is worth exploring the possibility of implementing such neural network models to correctly predict the behaviour of infilled structures. Moreover, the investigation is carried out covering a wide range of existing steel moment frames, including low-rise and mid-rise buildings designed to low and high seismicity, such that the applicability of the proposed method is also demonstrated.

3. Neural network classification models

3.1. Network structure

Artificial neural networks (ANNs) are computing systems developed to imitate the way human brains process information and perform tasks including pattern recognition, data classification and forecast of future events. A feedforward neural network (FNN) is a typical type of ANNs that contains one input layer, one or a few hidden layers and one output layer, whose structure are demonstrated in Fig. 1. It is worth noting that in fully connected FNN models, each node is fully connected with the nodes in its adjacent layers and data are only allowed to move forward from the input layer to the output layer through the hidden layer.

The input and hidden layers of FNN classification models usually have the same features as regression models. As can be seen in Fig. 1, the input layer is where the predictor data are provided to the FNN model, and then standardised before being sent to the hidden layers for further

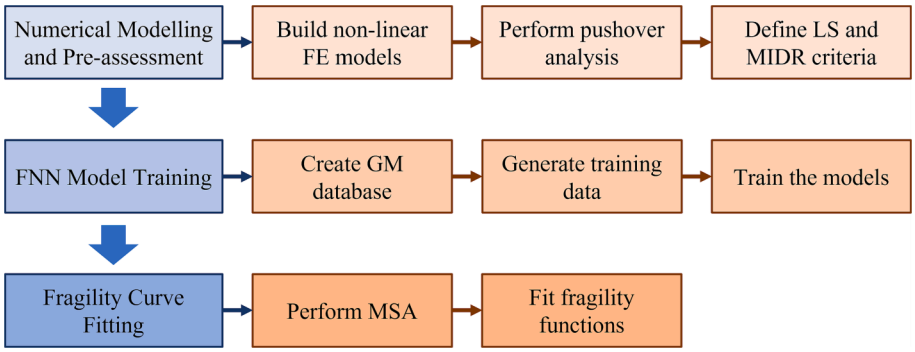

Fig. 2. The proposed framework for deriving fragility curves of existing steel frames with masonry infills.

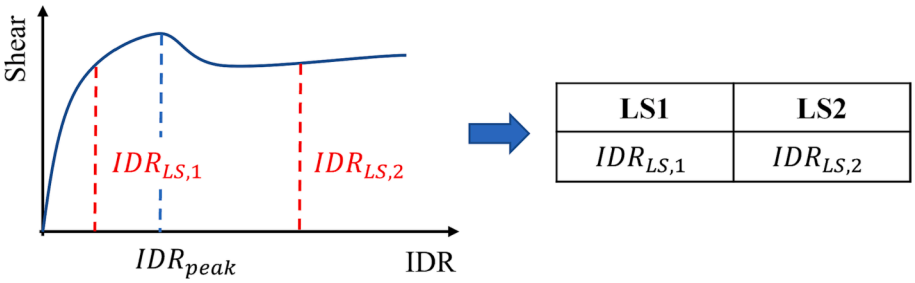

Fig. 3. Definition of limit states and IDR criteria based on the pushover curve.

processing. Then at the hidden layer, weights and bias are applied to the signal from the input layer. The use of activation function is also required aiming at introducing nonlinearity into the network models to enhance their capabilities of solving nonlinear problems [15]. Some frequently used activation functions in the hidden layer are presented in Fig. 1, including the rectified linear unit (ReLU) function, the hyperbolic tangent (tanh) function and the sigmoid function.

The major difference between FNN classification models and regression models is in the output layer. FNN classification models rely on the softmax function to make predictions based on the posterior probability of each output, i.e. the output corresponding to the largest posterior probability is adopted as the predicted class. The softmax function is illustrated in Eq.(1), where K is the number of class considered in the classification problem and the sum of posterior probabilities p_i from each output node should always be equal to unity.

$$p_i = f(z_i) = \frac{e^{z_i}}{\sum_{j=1}^{K} e^{z_j}} \tag{1}$$

3.2. Training algorithm and performance evaluation Parameter:

The training of FNN models involves two essential aspects, namely the training algorithm and the performance evaluation parameter. In the present study, the limited-memory Broyden-Fletcher-Goldfarb-Shanno quasi-Newton algorithm (LBFGS) [31] is adopted as the training algorithm, which uses the Hessian matrix approach instead of the Jacobian matrix approach used by Newton method to reduce the time required to perform the optimisation task. Besides, the LBFGS algorithm only uses a limited amount of computer memory, as it utilises a matrix with reduced size compared to the one used by the original BFGS method to approximate the inverse Hessian matrix.

The LBFGS algorithm optimises the FNN models based on the cross-entropy loss, which indicates the predictive inaccuracy of the FNN classification models, as defined by Eq. (2), where the indicator y_j is equal to unity for the posterior possibility p_j corresponding to the true observed class and otherwise equal to zero.

$$\text{Loss} = -\frac{1}{n}\sum_{i=1}^{n}\left(\frac{1}{K}\log\left(\sum_{j=1}^{K} y_j p_j\right)\right) \tag{2}$$

The training of FNN models is usually based on two sets of data, which are the training data and the validation data. As suggested by the names, the FNN models learn from the training data, based on which the model properties are defined, including the weights and biases. On the other hand, the use of validation data is to accelerate the training process and to prevent over-fitting, particularly when a limited size of training data is adopted.

4. Proposed framework for deriving fragility curves

The proposed framework for deriving fragility curves is introduced in this section. The framework contains three main steps, as demonstrated in Fig. 2, which includes numerical modelling and pre-assessment of the infilled steel frames, training of the FNN models and lastly, the derivation of fragility curves. Details of the framework are described herein.

4.1. Numerical modelling and pre-assessment

The first step of the proposed framework is to build the finite element (FE) model and conduct preliminary assessment of the steel frame to be investigated, as demonstrated in Fig. 3. This step is aimed to define appropriate limit states and the corresponding inter-storey drift ratio (IDR) limits for the derivation of state-dependent fragility curves.

This step further involves three sub-steps. The first is to build the FE model appropriate for dynamic (time-history) analysis, where the cyclic behaviour of the model should reflect properly the degradation of stiffness and strength of the structure. Then the monotonic behaviour of the subject structure at the storey level can be acquired by performing pushover analysis. A typical storey shear-IDR curve of infilled existing steel frames is shown in Fig. 3, where a clear drop of shear force can be seen after the peak strength point due to failure of masonry infills. Finally, based on the results of pushover analysis, building-specific limit

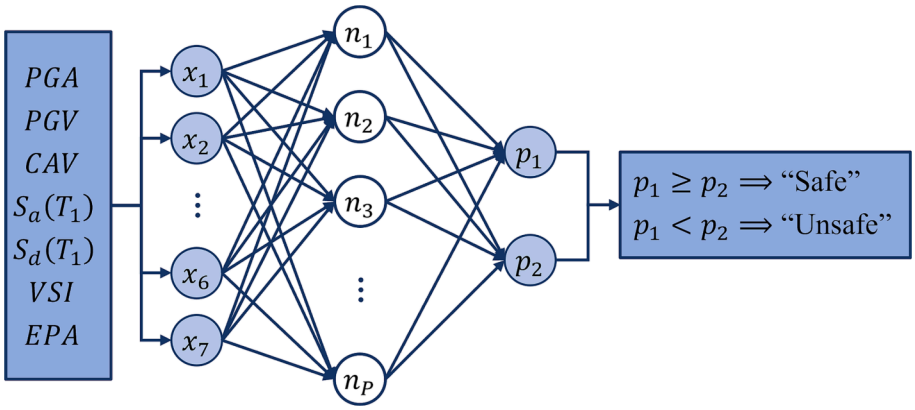

Fig. 4. The structure of a feedforward neural network model with single hidden layer.

Table 1
Intensity measures of the GMs involved in the development of FNN models as input parameters.

Notation	Intensity measure	Formula
PGA	Peak ground acceleration	$\max(\lvert\ddot{x}_g\rvert)$
PGV	Peak ground velocity	$\max(\lvert\dot{x}_g\rvert)$
CAV	Cumulative absolute velocity	$\int_0^t \lvert\ddot{x}_g\rvert \, dt$
$S_a(T_1)$	Spectral acceleration at T_1	$S_a(T_1)$
$S_d(T_1)$	Spectral displacement at T_1	$S_d(T_1)$
VSI	Velocity spectrum intensity	$\int_{0.1}^{2.5} S_v \, dT$
EPA	Effective peak ground acceleration	$\frac{\overline{S_a(0.1,\cdots,0.5)}}{2.5}$

states can be defined by assessing the damage state of the structure at increasing lateral displacement. Alternatively, codified limit states and IDR criteria may also be adopted depending on the scope of research.

4.2. Training of FNN models

The second step is to prepare the training data and establish the FNN models. A schematic diagram showing the structure of the FNN models adopted in this study is provided in Fig. 4, where it can be seen that the input parameters contains seven representative intensive measures (IMs) of GMs based on the suggestions from previous studies [15,35]. Also, the proposed structure of the FNN model was initially selected based on the recommendation from the previous study performed by Morfidis and Kostinakis [15]. In the meantime, due to the lack of direct method for the determination of optimal number of hidden nodes (denoted as n_p in Fig. 4), a trial and error tests were conducted, which suggested that 10 to 20 hidden nodes were generally sufficient for the proposed work.

The selected IMs were listed in Table 1, including peak ground acceleration (PGA), peak ground velocity (PGV) and cumulative absolute velocity (CAV), which are determined directly from the time history of the ground motion records, and spectral acceleration at T_1 ($S_a(T_1)$), spectral displacement at T_1 ($S_d(T_1)$), velocity spectrum intensity (VSI) and effective peak ground acceleration (EPA), which can be determined from the response spectra of the records.

To prepare the training data, a suite of GM records should initially be selected. In the present study, the GM records adopted by FEMA P695 [36] are used as the standard GM record database, which comprises 28 near-fault GMs and 22 far-field GMs. Subsequently, three sets of data are to be generated within this step to serve as the training data, as demonstrated in Fig. 5, which correspond to three different scaling factors applied to the selected GM records. For each scaling factor, the maximum IDRs (MIDRs) of the structure should be determined through NTHA, and then labelled as 'Safe' or 'Unsafe' based on the target limit state to form the output of the training data, while the input data are the corresponding IMs summarised in Table 1.

It should also be noted that the scaling factor SF_1 is computed based on Eq.(5), which is the ratio between the target IDR limit (IDR_{LS}) and the

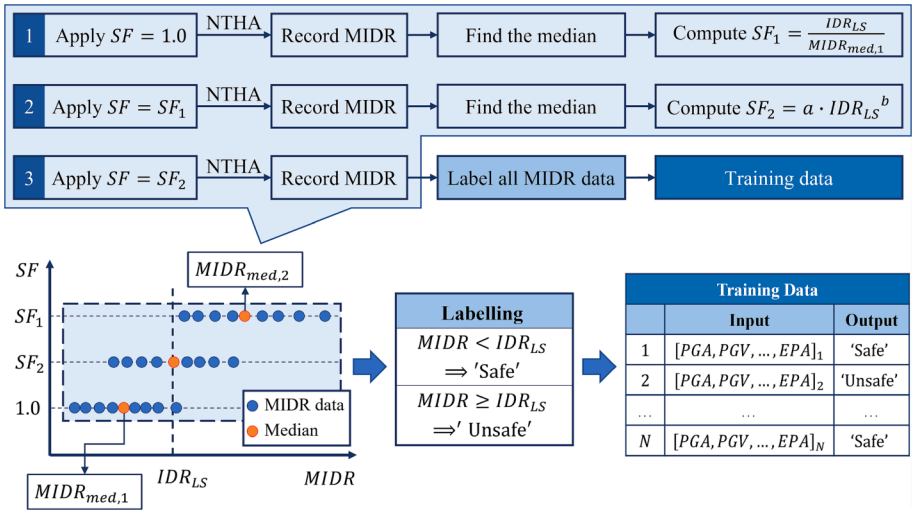

Fig. 5. The procedure of generating the training and validation datasets.

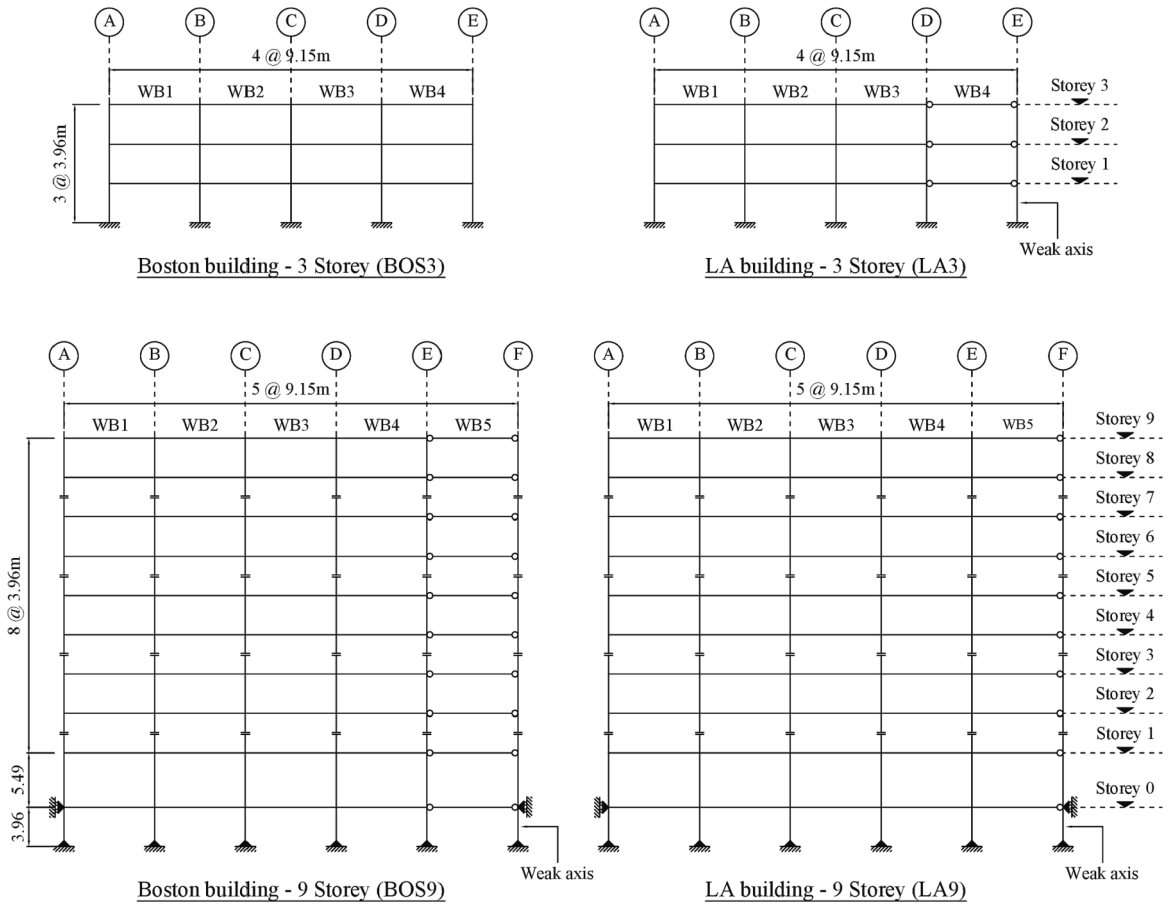

Fig. 6. Geometry properties of the case study steel buildings and element profiles.

Table 2
Beam and column profiles for the BOS3 building.

'Floor	Column	Beam	
	A, E	B, C, D	WB1
1	W14 × 74	W14 × 99	W21 × 62
2	W14 × 74	W14 × 99	W21 × 57
3	W14 × 74	W14 × 99	W18 × 35

median of the MIDRs recorded for unscaled GM records ($MIDR_{med,1}$). On the other hand, the scaling factor SF_2 is determined based on Eq. (6), where the coefficients a and b define the exponential function passing through the nodes ($MIDR_{med,1}$, 1.0) and ($MIDR_{med,2}$, SF_1), with $MIDR_{med,2}$ being the median of the MIDRs recorded for the GM records scaled by SF_1. Due to the nonlinearity of structures, the value of SF_2 should be between 1.0 and SF_1, but the value of SF_1 can be smaller than 1.0. Eventually, the dataset with respect to the scaling factors 1.0 and SF_1 are combined to be the training data, whereas the dataset with respect to the scaling factor SF_2 is adopted as the validation data, thus the ratio between the size of training and validation is set to be equal to 2:1.

$$SF_1 = \frac{IDR_{LS}}{MIDR_{med,1}} \tag{5}$$

$$SF_2 = a \bullet IDR_{LS}{}^{b} \tag{6}$$

4.3. Derivation of fragility curves

The last step of the proposed framework is to derive the fragility curves by performing MSA [4]. Instead of performing additional NTHA, the trained FNN models are used to predict explicitly whether the structure is safe or not subjected to each input IM combination. In addition, to avoid complicating the problem, the IM combinations extracted from the selected natural GM records are adopted directly as the input data during the MSA, in which case the correlations among adopted IMs need not be clarified as in the case of Monte Carlo simulation. Eventually, the fitting of fragility curves can be achieved based on the least squares or the maximum likelihood method.

5. The case study buildings

To demonstrate the proposed method for deriving fragility curves, four pre-Northridge buildings from the SAC Steel Project [32] were adopted as the case study buildings. The steel buildings selected for this study are the 3- and 9-storey buildings, which were designed following the local seismic codes in Boston and Los Angeles, respectively. Therefore, the Boston buildings are representatives of the steel buildings designed for low-seismicity, whilst the Los Angeles buildings represent buildings designed for high-seismicity. It is worth mentioning that the four buildings were selected for the present study because they have been widely accepted as case study buildings in previous research e.g., [32,33], hence were considered appropriate representatives of existing steel buildings in the United States. For convenience, the four buildings are hereafter referred to as BOS3, BOS9, LA3 and LA9, respectively for the 3- and 9-storey Boston and Los Angeles buildings.

Due to the regularities of the steel buildings in the plan layouts and along the heights, only their perimeter frames in the N—S direction were considered in this study, which are shown in Fig. 6, as the internal gravity frames were not considered to contribute significantly to the lateral resistance of the buildings. The profiles of beams and columns are

Table 3
Beam and column profiles for the LA3 building.

Floor	Column	Beam			
	A, D	B, C	E	WB1	WB2
1	W14 × 257	W14 × 311	W14 × 68	W33 × 118	W21 × 44
2	W14 × 257	W14 × 311	W14 × 68	W30 × 116	W21 × 44
3	W14 × 257	W14 × 311	W14 × 68	W24 × 68	W21 × 44

Table 4
Beam and column profiles for the BOS9 building.

Floor	Column	Beam			
	A	B, C, D, E	F	WB1	WB2
0	W14 × 211	W14 × 283	W14 × 211	W24 × 68	W24 × 68
1	W14 × 211	W14 × 283	W14 × 211	W36 × 135	W27 × 94
2	W14 × 159	W14 × 233	W14 × 159	W33 × 118	W27 × 84
3	W14 × 159	W14 × 233	W14 × 159	W30 × 116	W27 × 84
4	W14 × 132	W14 × 211	W14 × 132	W30 × 116	W24 × 76
5	W14 × 132	W14 × 211	W14 × 132	W30 × 108	W24 × 76
6	W14 × 99	W14 × 176	W14 × 99	W30 × 99	W24 × 68
7	W14 × 99	W14 × 176	W14 × 99	W27 × 94	W24 × 62
8	W14 × 61	W14 × 120	W14 × 68	W24 × 76	W24 × 55
9	W14 × 61	W14 × 120	W14 × 68	W18 × 40	W18 × 40

Table 5
Beam and column profiles for the LA9 building.

Floor	Column	Beam	
	A, F	B, C, D, E	WB1
0	W14 × 370	W14 × 500	W36 × 160
1	W14 × 370	W14 × 500	W36 × 160
2	W14 × 370	W14 × 455	W36 × 160
3	W14 × 370	W14 × 455	W36 × 135
4	W14 × 283	W14 × 370	W36 × 135
5	W14 × 283	W14 × 370	W36 × 135
6	W14 × 257	W14 × 283	W36 × 135
7	W14 × 257	W14 × 283	W30 × 99
8	W14 × 233	W14 × 257	W27 × 84
9	W14 × 233	W14 × 257	W24 × 68

provided in Tables 2–5. The nominal yield strength of columns is 344.5 MPa for all four buildings, whilst the nominal yield strength of beams is 248.0 MPa for Los Angeles buildings and 344.5 MPa for Boston buildings. Fully welded pre-Northridge beam-column connections are used in the moment frames, but it should be noted that the BOS9, LA3 and LA9 buildings all comprise a bay with pinned beam-column connections. The BOS3 and LA3 buildings are fixed at the base, while the BOS9 and LA9 buildings have pinned column base connections. Moreover, as can be seen in Fig. 6, both of the two 9-storey buildings have a basement floor, hence lateral constraints are also considered at the ground level of the two buildings in addition to the constraints at column bases.

6. Implementation of the proposed method

6.1. FE modelling of the steel buildings

2D-FE models of the case study buildings were implemented in OpenSees [34]. The FE model of the LA3 building is shown in Fig. 7 as an example of the modelling scheme, where it can be seen that the FE model consisted of two parts, the 'Steel Frame' and the 'Leaning Column'. All beams and columns of the steel frame were modelled using force-based beam-column elements with fibre sections, whose properties were defined by the Steel01 material from the OpenSees material library. Besides, instead of using the nominal yield strength of the steel, i.e. 248.0 and 344.5 MPa, the corresponding expected values of the yield strength were adopted, i.e. 339.0 and 396.9 MPa, as suggested by Gupta and Krawinkler [32], as well as a hardening ratio of 0.02. Furthermore, the fully welded beam-column connections were assumed to be rigid in the FE models, while the pinned beam-column connections were modelled using a rotational spring with negligible stiffness. Lastly, the aforementioned boundary conditions were implemented in the FE models, including the lateral restraints applied at the ground level of the BOS9 and LA9 buildings.

An essential part of the FE models is the modelling of masonry infills. In the present study, the masonry infills were modelled using the Liberatore-Decanini approach [30], which is illustrated in Fig. 8a. The model contained a single compression-only strut in each diagonal direction to simulate the infill wall panels, and the mechanical properties of the strut was described by a four-branch multilinear curve. Since no information of masonry infills was provided in the original document of the four steel buildings, the material properties utilised to define the single-strut model were assumed according to a previous experimental test on infilled existing steel frame [24]. The Young's modulus E_m was 7669 MPa, the vertical compression strength f_m was 2.81 MPa and the tensile strength obtained from diagonal compression tests f_t was 0.65 MPa. The properties of the masonry struts were defined using the Hysteretic material in OpenSees, with assumptions also made in relation to the pinching of the masonry infills. Fig. 8b shows an example of the cyclic behaviour of the masonry struts. The thickness of infill walls in the BOS3 and LA3 buildings, as well as on the top five storeys of the BOS9 and LA9 buildings, was assumed to be 155 mm. For the bottom five storeys of the BOS9 and LA9 buildings, the thickness of infills was assumed to be 233 mm. In addition to the steel frame structures, leaning columns were also introduced to the FE models to account for the P-

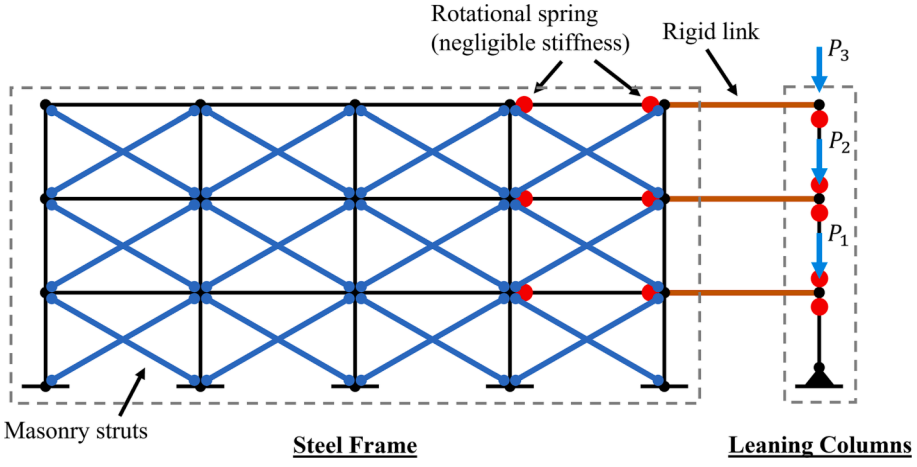

Fig. 7. Illustration of the FE modelling in OpenSees: the LA3 building.

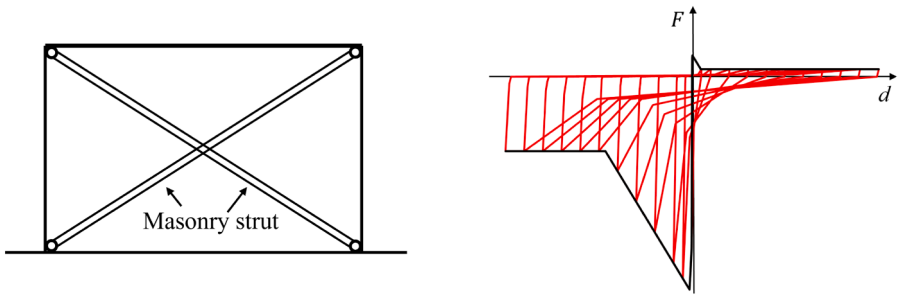

Fig. 8. Demonstration of the Libertore-Decanini model [30] for masonry infills.

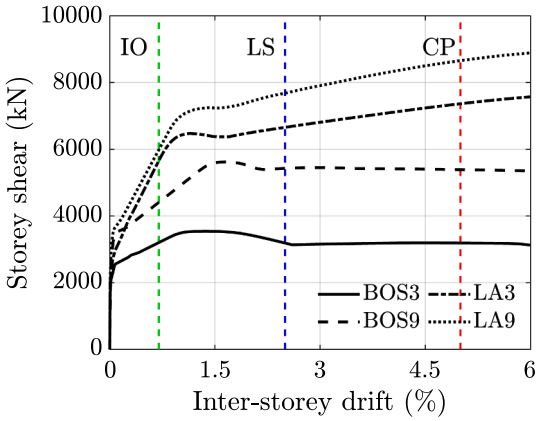

Fig. 9. Pushover curves of the case study buildings at the storey level.

Table 6
The IDR criteria recommended by FEMA 365 [38].

Limit state	IDR (%)	Description
IO	0.7	Minor local yielding at a few places; No fractures; Minor buckling or observable permanent distortion of members.
LS	2.5	Hinges form; Local buckling of some beam elements; Severe joint distortion; A few elements may experience partial fracture.
CP	5.0	Extensive distortion of beams and column panels; Many fractures at moment connections.

Table 7
Median MIDRs and scaling factors adopted to generate the training data.

		BOS3	BOS9	LA3	LA9
Unscaled	$MIDR_{med,1}$ (%)	0.983	0.720	0.483	0.567
IO limit state	$MIDR_{med,2}$(%)	0.578	0.707	0.912	0.742
	SF_1	0.712	0.973	1.449	1.234
	SF_2	0.805	0.956	1.242	1.179
LS limit state	$MIDR_{med,2}$(%)	4.952	4.100	5.686	3.790
	SF_1	2.542	3.474	5.175	4.408
	SF_2	1.714	2.438	2.992	3.185
CP limit state	$MIDR_{med,2}$(%)	17.288	9.706	12.861	8.838
	SF_1	5.085	6.948	10.350	8.816
	SF_2	2.516	4.239	5.281	5.613

Delta effect, as demonstrated in Fig. 7. The leaning columns were modelled by rigid beam elements and were connected to the main structure through rigid truss elements (rigid links in Fig. 7). Since the leaning columns were included only to account for the P-Delta effect, they were assumed to be not capable of transferring bending moment. Thus, rotational springs with negligible stiffness were also added to the ends of leaning column to release the moment at joints. A pinned end was assumed at the base of leaning columns in all FE models.

The storey masses were assigned to each node in the main structures based on their tributary areas, i.e. the corner nodes were assigned half the mass of the intermediate nodes. No mass was added to the nodes in the leaning columns. On the other hand, gravity loads were applied to both the steel frame and the leaning column in each FE model. The gravity loads, which in reality were sustained by the internal gravity frames, were applied to the corresponding nodes in the leaning column, as shown in Fig. 7. In the meantime, the gravity loads added to the steel frame in each FE model were solely the gravity loads sustained by the frame structure, which were less significant compared to the gravity loads on the leaning column, hence are not shown in Fig. 7 for clarity.

6.2. Assessment of the seismic behaviour of the steel buildings

Pushover analysis was performed at the beginning as a preliminary assessment of the case study buildings. The pushover curves of the case study buildings are presented in Fig. 9, in terms of the base shear against the inter-storey drift ratio. The curves shown in Fig. 9 were extracted from the floor where soft-storey mechanism occurred during the push-over analysis, i.e. the ground floor for of the BOS3 and LA3 building and the third floor of the BOS9 and LA9 building. It is clearly shown by the pushover curves that the presence of masonry infills is able to cause more complex inelastic behaviour of the steel buildings, hence leads to increased difficulty in the establishment of the FNN models and estimating accurately the structural response.

6.3. Definition of limit states and IDR criteria

To demonstrate the proposed method, three codified limit states recommended by FEMA 365 [38] were adopted in this case study. The corresponding IDR limits are presented in Table 6, which are 0.7, 2.5 and 5.0 %, respectively for the Immediate Occupancy (IO), Life Safety (LS) and Collapse Prevention (CP) limit state. Alternative building specific IDR limits defined based on the pushover curves of structures may also be used in order to achieve higher accuracy in the obtained fragility curves, but in the present study the standardised criteria in Table 6 was adopted for illustration purpose.

6.4. Selection of ground motions and intensity measures

As mentioned in Section 4, the GM database in FEMA P695 [36] was adopted to generate the training data, which were obtained from the PEER database [37]. It should be mentioned that the GM database originally contained 28 near-fault GMs and 22 far-field GMs, however, one of the far-field GMs was missing from the PEER database and was excluded from the present study, leading to a database of 49 GM records.

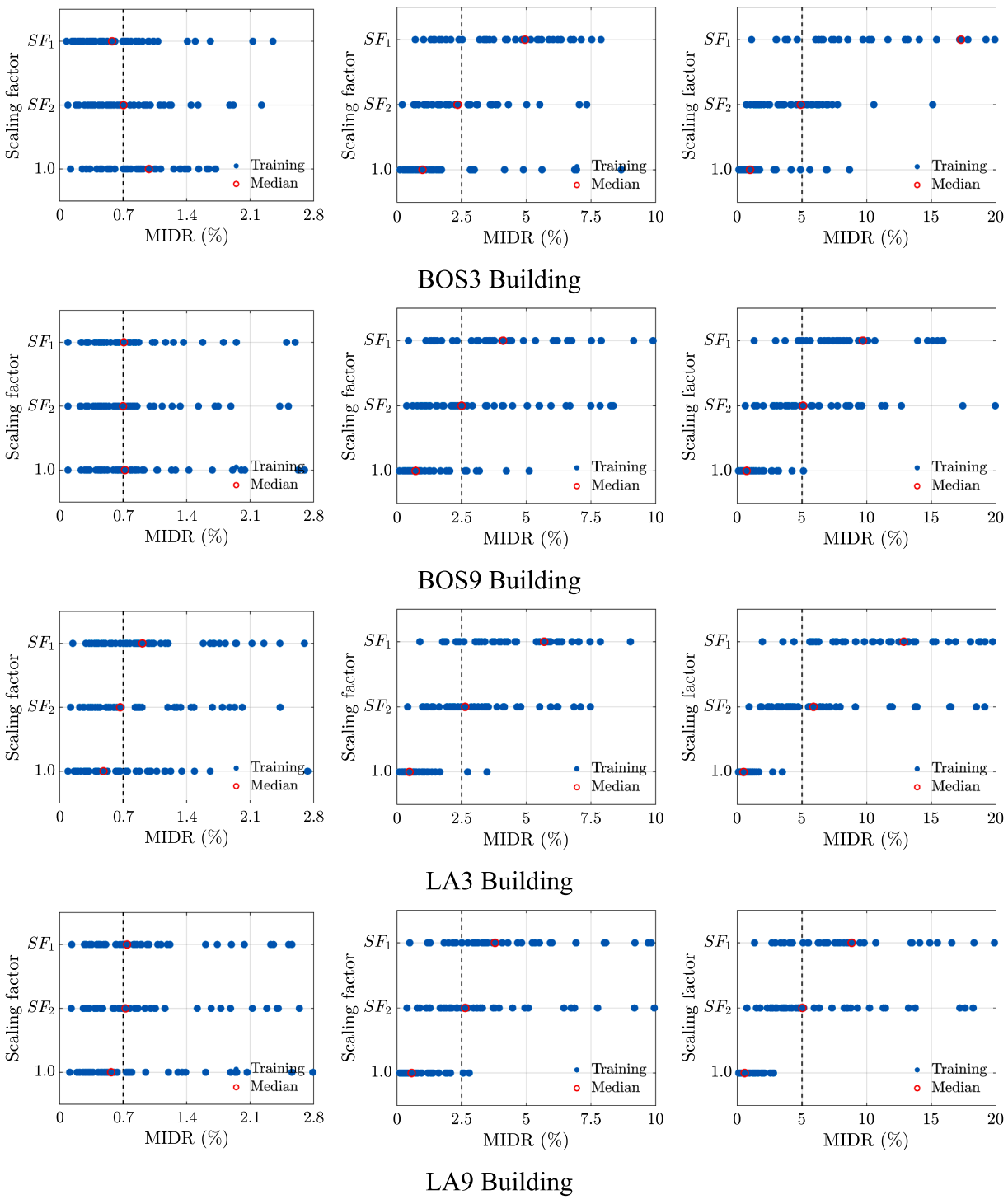

Fig. 10. Distribution of the training data generated for each case study steel frame with respect to the target IDR limit (indicated as the black dash line).

Besides, only the first horizontal component of each ground motion was considered in this study for the development of fragility curves for the demonstration of the proposed method. It should also be noted that the two database of near-fault and far-field GM records were not considered individually herein, as the purpose of this study was not to investigate the structural behaviour subjected to near-fault and far-field ground motions, but to show the capability of the proposed method in dealing an ordinary suite of selected GM records which does not separate near-fault or far-field GMs.

6.5. *Preparation of training data*

The procedure of generating training and validation datasets proposed in Section 4.2 were repeated for each steel building at each limit state. The median MIDRs and scaling factors calculated to scale the GM records were summarised in Table 7. Fig. 10 shows the data generated for training the FNN models based on the scaling factors in Table 7. As can be seen, the definition of SF_1 effectively led to a group of MIDR data that in combination with the unscaled MIDRs forming a balanced training dataset, due to the significant nonlinearity of the structural response. It should be mentioned that in this case, 'balanced data' does

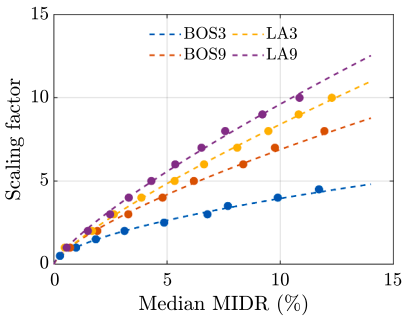

$$\text{BOS3: } y = 1.028x^{0.585} \ (R^2 = 0.995)$$

$$\text{BOS9: } y = 1.313x^{0.720} \ (R^2 = 0.997)$$

$$\text{LA3: } y = 1.346x^{0.800} \ (R^2 = 0.999)$$

$$\text{LA9: } y = 1.570x^{0.787} \ (R^2 = 0.997)$$

Fig. 11. Exponential relationship between the scaling factor and the median MIDR.

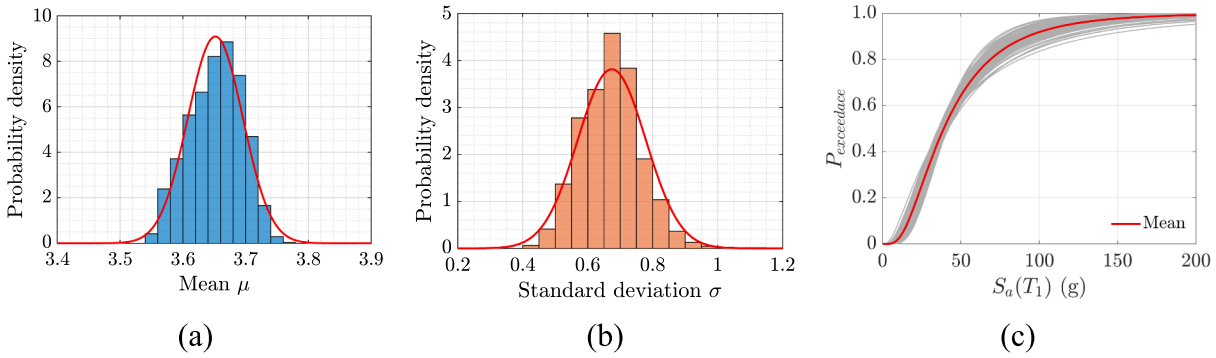

Fig. 12. Training of FNN models (BOS9 building at CP limit state): (a) distribution of the mean (μ); (b) distribution of the standard deviation (σ); (c) the mean fragility curve.

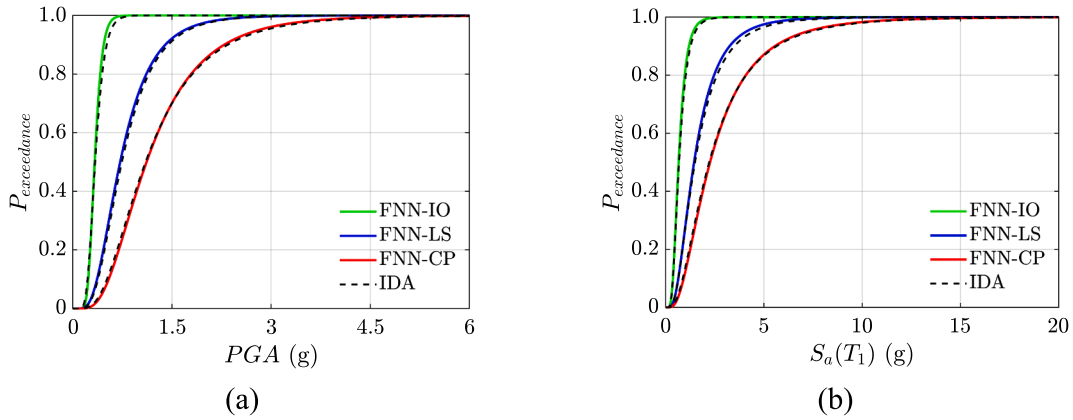

Fig. 13. Fragility curves of BOS3 building using PGA (a) and $S_a(T_1)$ (b) as the IM.

not require equally divided MIDR data, but the numbers of data leading to 'Safe' and 'Unsafe' cases are not supposed to considerably differ from each other.

The use of an exponential expression for the definition of SF_2 is explained in Fig. 11, which shows clearly that the relationship between the median MIDR based on the selected GM database and the scaling factor can be well approximated by an exponential curve for all the steel frames in this study. Additionally, it is also shown in Fig. 10 that the adopted SF_2 effectively led to median values of MIDR approximately equal to the target IDRs, suggesting that the validation data were also balanced.

Furthermore, as shown in the case of BOS9 and LA9 buildings at the IO limit state in Fig. 10, the median of the obtained MIDRs under unscaled GM records ($MIDR_{med,1}$) can be close to the target IDR (IDR_{LS}), in which cases the scaling factors SF_1 and SF_2 are likely to be equal to one. As a consequence, the patterns of the data obtained with the scaling factor 1.0 (unscaled), SF_1 and SF_2 can be similar to each other, which may lead to repeated training data and compromised accuracy of the trained FNN models. However, as this circumstance is not frequent and can be easily addressed by applying a suitable scaling factor instead of 1.0 to generate the first dataset, it is considered not affecting significantly the capability of the proposed framework.

6.6. Training of the FNN models

Prior to the training of the FNN models, a few times of trial training were conducted and it was found that a hidden layer with eight nodes was sufficient in this study to allow adequate accuracy of the FNN models for all case study buildings. The ratio between the sizes of training and validation data was 2:1 as described in Section 4.2.

It is worth mentioning that for each building and limit state under consideration, the trained FNN models are not unique due to the sto-

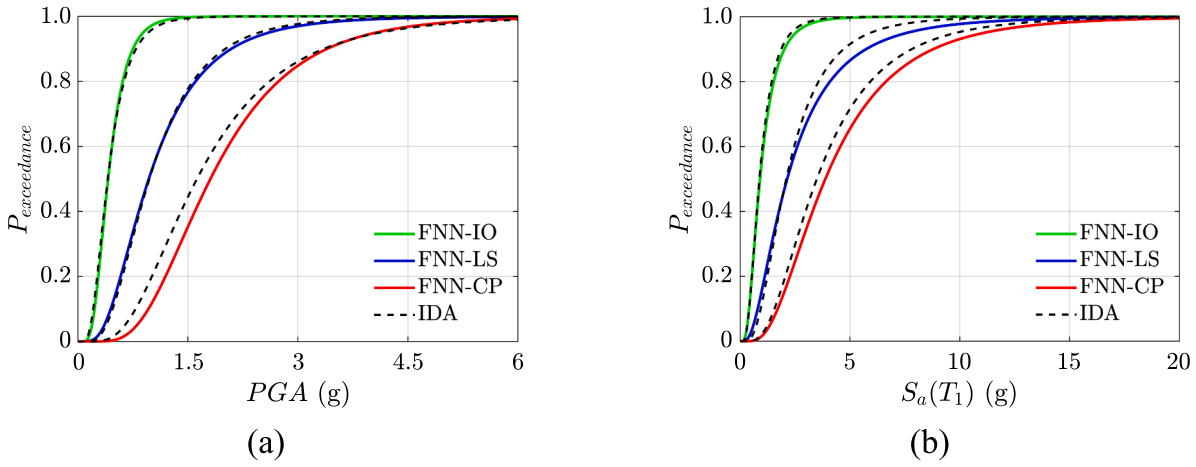

Fig. 14. Fragility curves of BOS9 building using PGA (a) and $S_a(T_1)$ (b) as the IM.

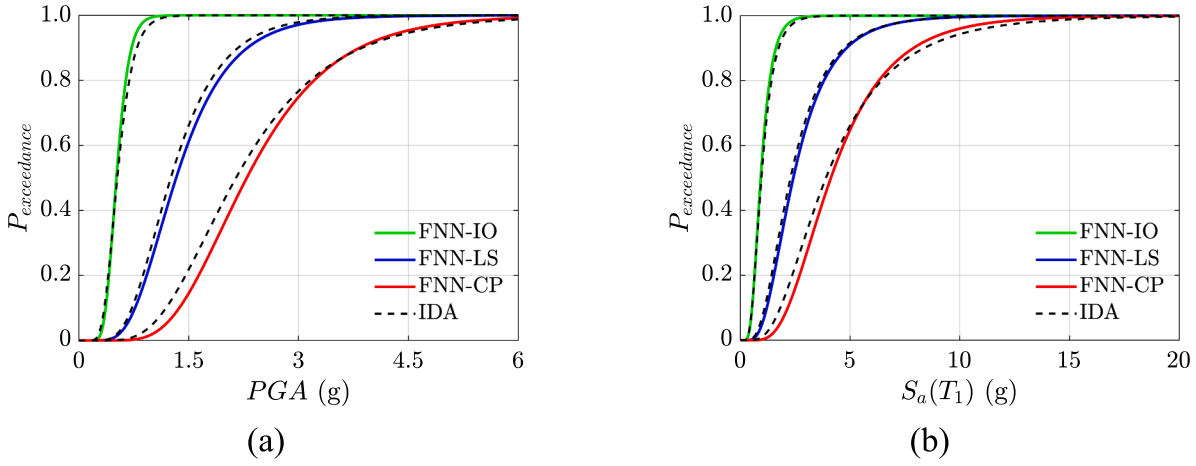

Fig. 15. Fragility curves of LA3 building using PGA (a) and $S_a(T_1)$ (b) as the IM.

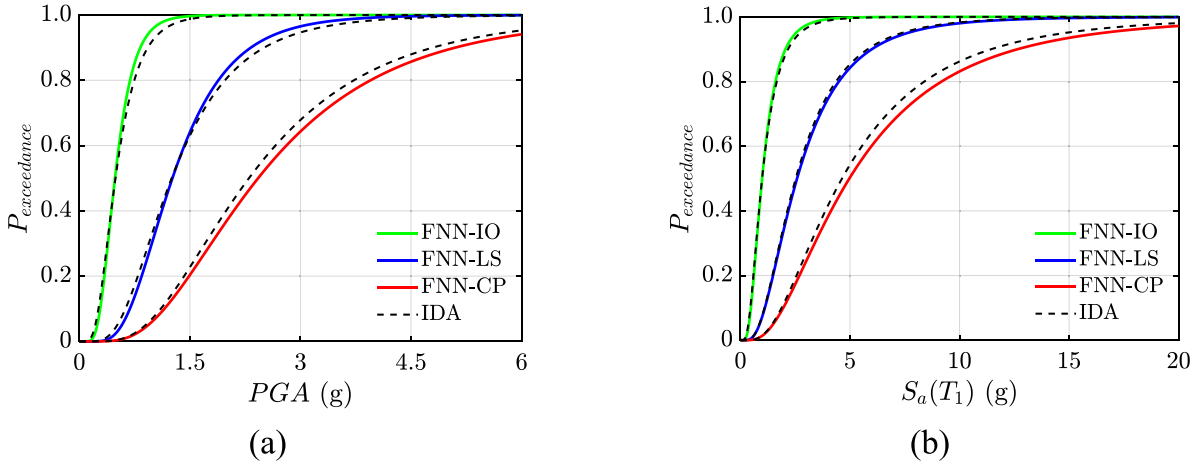

Fig. 16. Fragility curves of LA9 building using PGA (a) and $S_a(T_1)$ (b) as the IM.

chastic training algorithm, thus the resultant fragility curves are not unique, either. Nonetheless, it was also noticed that the trained FNN models would most likely to yield very similar results, despite significantly different results might occur from time to time. This is illustrated in Fig. 12a and b, which respectively show as an example the distribution of the mean (μ) and standard deviation (σ) generated from 10,000 trained FNN models for the BOS9 building at the LS limit state using $S_a(T_1)$ as the IM. Based on this observation, a single best estimate of the fragility curve could be obtained by finding the mean values of the mean and standard deviation of all fragility curves generated, as illustrated in Fig. 12c. This can be achieved by simply taking the average of the results from sufficient number of trained FNN models, or more efficiently

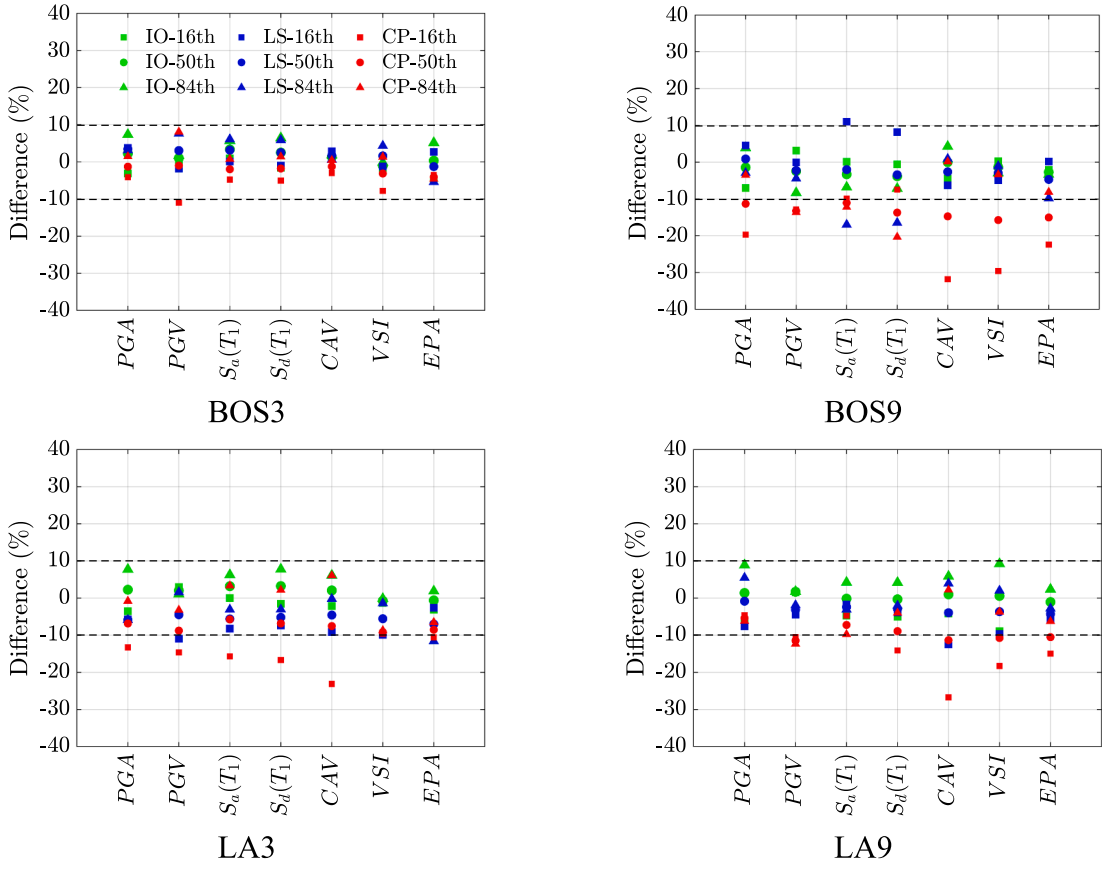

Fig. 17. Differences between the featured percentile values of the fragility curves obtained through the IDA and the FNN-based method w.r.t the IDA results.

Table 8
Total number of NTHA and time (in **minutes**) required to derive each fragility curves using the IDA and the proposed method.

Model	Limit state	IDA		Proposed			
		Standalone		Standalone		Cumulative	
		NTHA	Time	NTHA	Time	NTHA	Time
BOS3	IO	447	43	147	13	147	13
	LS	1005	95	147	13	245	22
	CP	1518	142	147	13	343	30
BOS9	IO	561	252	147	91	147	91
	LS	1314	596	147	91	245	152
	CP	2159	992	147	89	343	212
LA3	IO	673	72	147	17	147	17
	LS	1645	172	147	17	245	29
	CP	2796	288	147	17	343	40
LA9	IO	667	303	147	72	147	72
	LS	1668	769	147	72	245	120
	CP	3036	1401	147	74	343	170

Table 9
The elapsed time (in **seconds**) of the FNN model training session, including the iterative procedure for searching the parameters of mean fragility curve.

Model	Limit state	PGA	PGV	$S_a(T_1)$	$S_d(T_1)$	CAV	VSI	EPA
BOS3	IO	6	2	3	1	2	3	3
	LS	13	27	16	5	3	6	6
	CP	7	19	18	4	9	7	8
BOS9	IO	4	10	9	3	4	5	5
	LS	28	38	39	11	7	12	14
	CP	41	41	86	10	16	21	34
LA3	IO	7	4	4	1	1	2	2
	LS	6	16	21	3	4	7	11
	CP	24	18	29	3	3	9	11
LA9	IO	6	5	9	1	3	8	3
	LS	32	25	47	9	12	7	32
	CP	80	47	142	37	16	32	62

through a designated iteration process for rapid determination of the mean fragility curve. Moreover, it is also noteworthy that the FNN models, which failed to achieve an accuracy of 70 % in estimating either the 'Safe' or 'Unsafe' class against the validation dataset were abandoned due to low training quality.

7. Derivation and comparisons of fragility curves

In this section, comparisons were made between the fragility curves obtained through conventional incremental dynamic analysis (IDA) and the proposed FNN-based method using MSA. For both cases, the MIDR was adopted as the EDP. Besides, the accuracy of the proposed FNN-based method was also validated against all selected IMs within the framework, in order to illustrate the potential flexibility in the choice of IMs when using the proposed framework to derive fragility curves.

7.1. Incremental dynamic analysis

The IDA performed in this study considered the same GM records used to generate training data in the previous section and a small incremental step of 0.1 for the scaling factor (i.e. the scaling factor of 0.1, 0.2, … were used until the exceedance of the target limit state). Therefore, the adopted IDA was sophisticated and time-consuming, but was supposed to result in high accuracy of the fragility curves. The fragility curves obtained based on the IDA method are presented by dashed lines in Figs. 13–16.

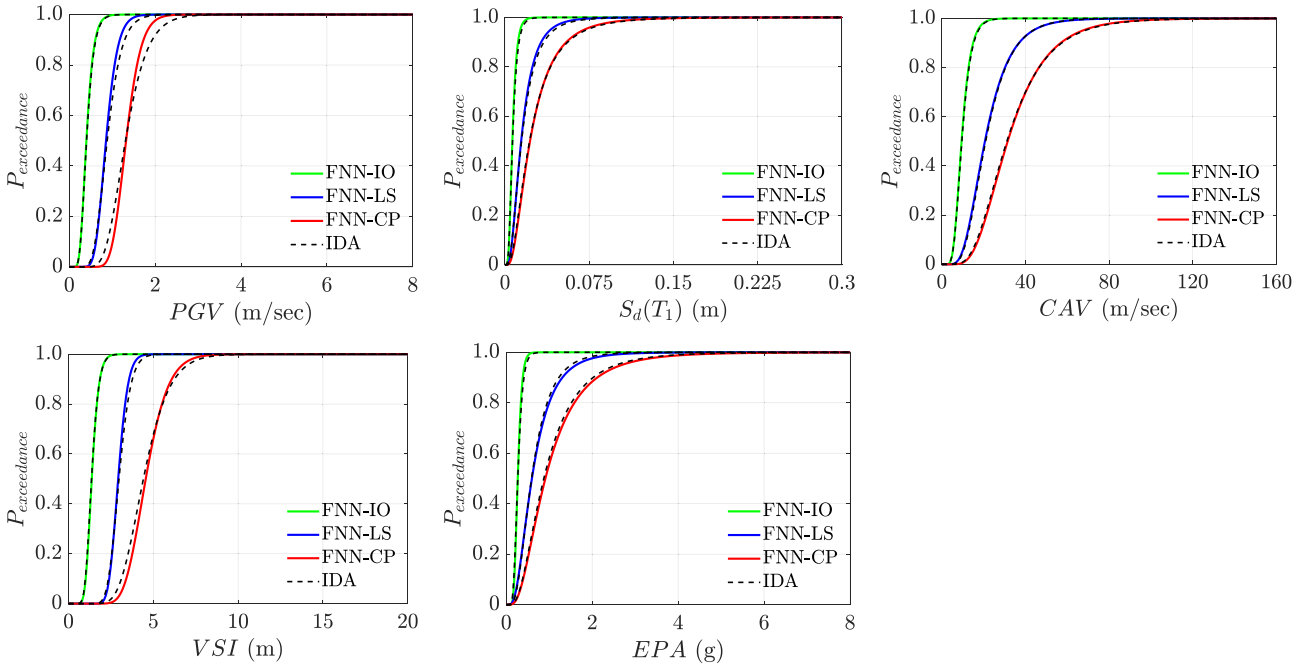

Fig. A1. Comparisons of fragility curves of the BOS3 building obtained using the proposed method with the IDA results.

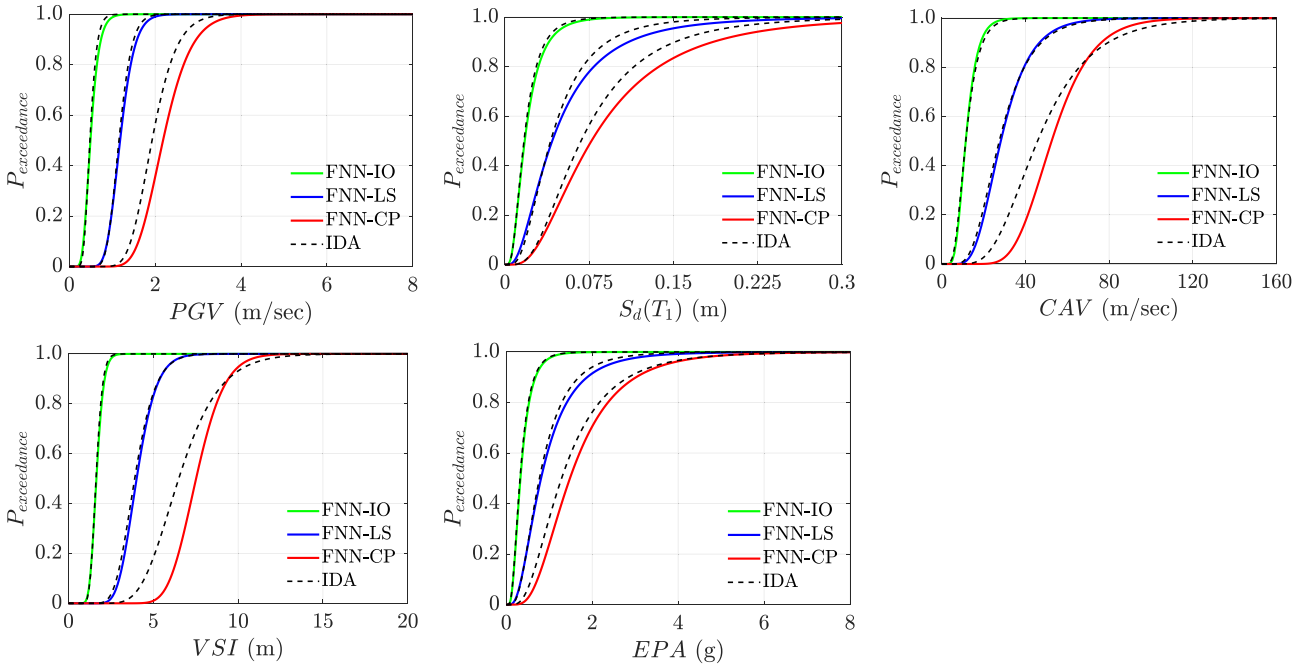

Fig. A2. Comparisons of fragility curves of the BOS9 building obtained using the proposed method with the IDA results.

7.2. The proposed FNN-Based method

The fragility curves obtained using the proposed FNN-based method using MSA were also presented in Figs. 13–16. For the sake of brevity, only the fragility curves obtained in terms of PGA and $S_a(T_1)$, the two most-widely adopted IMs, are present here, whereas the rest are provided in the appendix for completeness. By comparing the fragility curves obtained by the two methods, it can be seen that in general, the results obtained from the proposed method using FNN models provided a good approximation of the fragility curves obtained from the IDA. More specifically, the differences between the results were quantified by comparing the 16th, 50th and 84th percentile values of all fragility curves obtained, which are summarised in Fig. 17. It can be seen that in the majority of cases, the differences were within 10 %, regardless of IMs, limit states or building models. Nonetheless, there were a few exceptions where the differences exceeded 20 %, which were mainly in the case of the BOS9 building at the CP limit state. This was attributed to the fact that the BOS9 building was designed for low-seismicity, hence would experience significant strength degradation under seismic loading, as demonstrated by the pushover curves in Fig. 9.

Additionally, to compare the computational cost demanded by the IDA and the proposed method, the number of NTHAs required and total time spent on the NTHAs were summarised in Table 8. In the table, ‘standalone’ indicates the number of NTHA required to derive each of

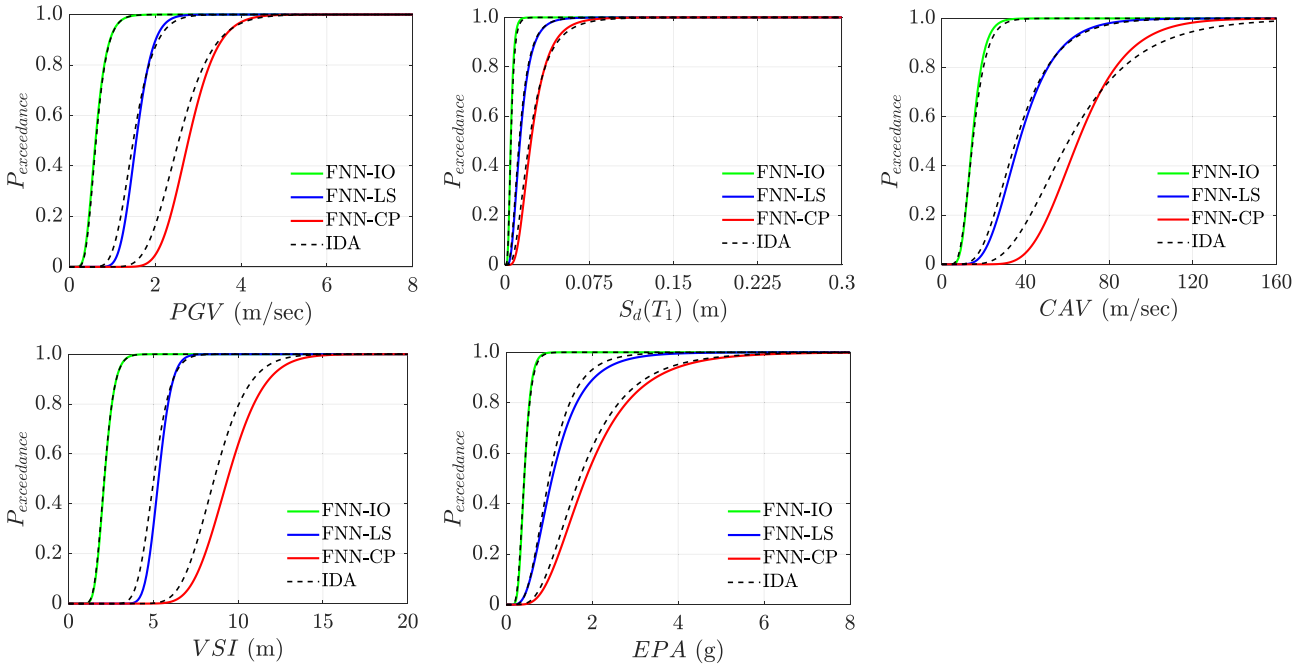

Fig. A3. Comparisons of fragility curves of the LA9 building obtained using the proposed method with the IDA results.

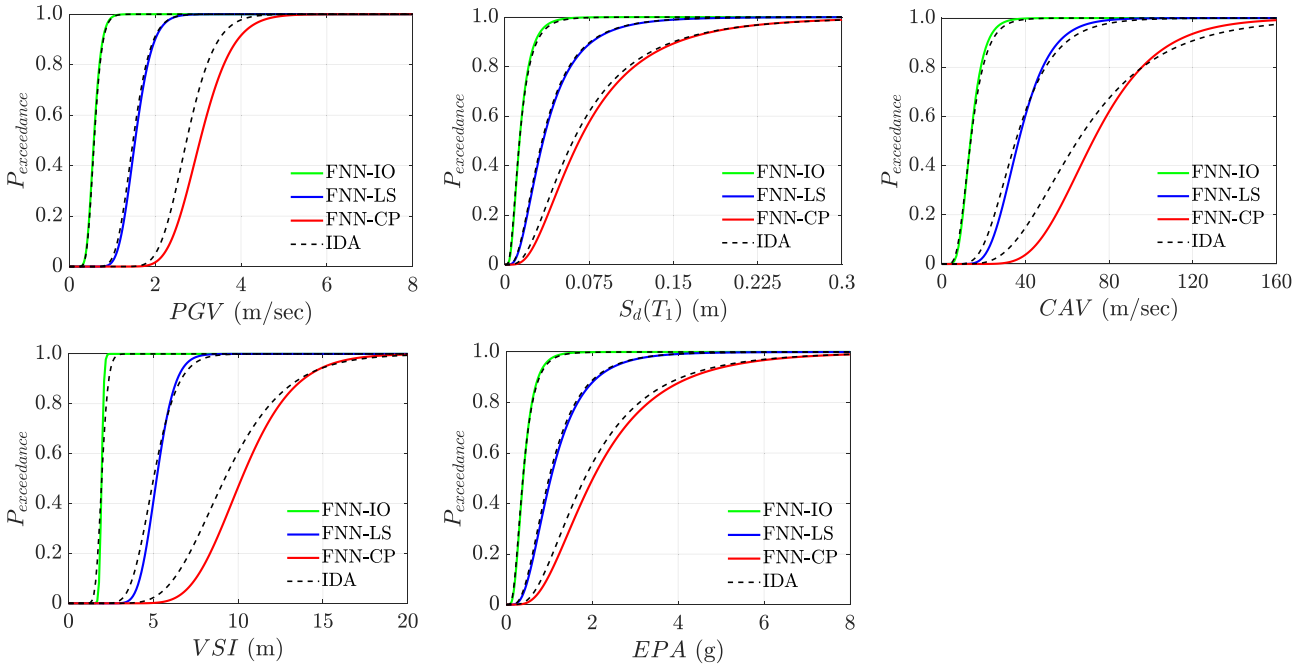

Fig. A4. Comparisons of fragility curves of the LA9 building obtained using the proposed method with the IDA results.

the corresponding fragility curve independently, while 'cumulative' indicates the cumulative number of NTHA required when deriving more than one state-dependent fragility curve simultaneously. Also, the time spent on the analyses referred to a mobile workstation with an Intel i7-10875H CPU comprising 8 cores/16 threads and 16.0 GB memory, which corresponded to a laptop for daily use rather than high-performance computing clusters. As shown in Table 8, the proposed method required significantly smaller numbers of NTHA and was time-saving compared to the IDA adopted in this study, particularly when the fragility curves corresponding to all limit states were of interest. On the other hand, the elapsed time of the FNN model training session, including the iterative procedure in Fig. 12, was provided in Table 9. It can be seen that nearly all the training sessions was completed within one minute, which were negligible compared to the time spent on the NTHAs. This also suggests that with an appropriate algorithm, the training of FNN models within the proposed framework can be done rapidly, allowing great potential of adopting FNN models in the seismic fragility analysis of existing steel buildings.

8. Conclusions

This paper presented a machine learning-based method to derive the fragility curves of existing steel frames, considering also the influence of masonry infills. The proposed method utilised FNN to estimate the

failure states of structures for the limit states under consideration, aiming at reducing considerably the computational cost as in the conventional IDA. Four steel moment frames were adopted as the case study buildings to demonstrate the proposed method, which were considered representatives of low- and mid-rise existing steel moment frames designed for low and high seismicity. Comparisons were made between the fragility curves obtained from conventional IDA using 49 GMs at small incremental steps, which was time-consuming but led to high accuracy of fragility curves, and the fragility curves obtained using the proposed method. The following conclusions can be drawn from the results:

- The fragility curves obtained using the proposed method were in general good approximation of the results obtained from the sophisticated IDA, especially when considering the influence of masonry infills on the overall structural response;
- Large differences between the results of the IDA and the proposed method were found to be in the case of the BOS9 building at CP limit state, as considering the superior limit state corresponding to the strength degradation stage of structural behaviour reduced the accuracy of the FNN models;
- The FNN models allowed flexibility in terms of the choice of IMs, as for the seven IMs considered in this study, the proposed method exhibited approximately the same performance in the derivation of fragility curves;
- The proposed method requested much less computational demand compared to the conventional IDA in terms of the number of required NTHAs and the time needed, whereas the time spent on the training of FNN models were negligible.

CRediT authorship contribution statement

Jing-Ren Wu: Conceptualization, Methodology. **Luigi Di Sarno:** Supervision, Resources.

Declaration of Competing Interest

The authors declare that they have no known competing financial interests or personal relationships that could have appeared to influence the work reported in this paper.

Data availability

The training data required to reproduce these findings are available as supplementary materials.

Appendix A

Figs. A1, A2, A3 and A4

Appendix B. Supplementary material

Supplementary data to this article can be found online at https://doi.org/10.1016/j.engstruct.2022.115345.

References

[1] Porter K, Kennedy R, Bachman R. Creating fragility functions for performance-based earthquake engineering. Earthq Spectra 2007;23(2):471–89. https://doi.org/10.1193/1.2720892.

[2] Elnashai AS, Di Sarno L. Fundamentals of earthquake engineering. 2nd ed. New Jersey: Wiley and Sons; 2015.

[3] Vamvatsikos D, Cornell CA. Incremental dynamic analysis. Earthq Eng Struct Dyn 2002;31(3):491–514. https://doi.org/10.1002/eqe.141.

[4] Baker JW. Efficient analytical fragility function fitting using dynamic structural analysis. Earthq Spectra 2015;31(1):579–99. https://doi.org/10.1193/021113EQS025M.

[5] Sun H, Burton HV, Huang H. Machine learning applications for building structural design and performance assessment: state-of-the-art review. J Build Eng 2021;33:101816. https://doi.org/10.1016/j.jobe.2020.101816.

[6] Murphy KP. Machine learning: a probabilistic perspective. Massachusetts: MIT Press; 2012.

[7] Mitropoulou CC, Papadrakakis M. Developing fragility curves based on neural network IDA predictions. Eng Struct 2011;33(12):3409–21. https://doi.org/10.1016/j.engstruct.2011.07.005.

[8] Xie Y, Ebad Sichani M, Padgett JE, DesRoches R. The promise of implementing machine learning in earthquake engineering: a state-of-the-art review. Earthq Spectra 2020;36(4):1769–801. https://doi.org/10.1177/8755293020919419.

[9] Falcone R, Lima C, Martinelli E. Soft computing techniques in structural and earthquake engineering: a literature review. Eng Struct 2020;207:110269. https://doi.org/10.1016/j.engstruct.2020.110269.

[10] Falcone R, Ciaramella A, Carrabs F, Strisciuglio N, Martinelli E. Artificial neural network for technical feasibility prediction of seismic retrofitting in existing RC structures. Structures 2022;41:1220–34. https://doi.org/10.1016/j.istruc.2022.05.008.

[11] Asteris PG, Mokos VG. Concrete compressive strength using artificial neural networks. Neural Comput Appl 2020;32(15):11807–26. https://doi.org/10.1007/s00521-019-04663-2.

[12] Asteris PG, Skentou AD, Bardhan A, Samui P, Lourenço PB. Soft computing techniques for the prediction of concrete compressive strength using Non-Destructive tests. Constr Build Mater 2021;303:124450. https://doi.org/10.1016/j.conbuildmat.2021.124450.

[13] Asteris PG, Lemonis ME, Le TT, Tsavdaridis KD. Evaluation of the ultimate eccentric load of rectangular CFSTs using advanced neural network modeling. Eng Struct 2021;248:113297. https://doi.org/10.1016/j.engstruct.2021.113297.

[14] Seo J, Dueñas-Osorio L, Craig JI, Goodno BJ. Metamodel-based regional vulnerability estimate of irregular steel moment-frame structures subjected to earthquake events. Eng Struct 2012;45:585–97. https://doi.org/10.1016/j.engstruct.2012.07.003.

[15] Morfidis K, Kostinakis K. Seismic parameters' combinations for the optimum prediction of the damage state of R/C buildings using neural networks. Adv Eng Softw 2017;106:1–6. https://doi.org/10.1016/j.advengsoft.2017.01.001.

[16] Moradi S, Burton HV. Response surface analysis and optimization of controlled rocking steel braced frames. Bull Earthq Eng 2018;16(10):4861–92. https://doi.org/10.1007/s10518-018-0373-1.

[17] Khojastehfar E, Beheshti-Aval SB, Zolfaghari MR, Nasrollahzade K. Collapse fragility curve development using Monte Carlo simulation and artificial neural network. Proc Inst Mech Eng Part O: J Risk Reliab 2014;228(3):301–12. https://doi.org/10.1177/1748006X13518524.

[18] Jough FK, Şensoy S. Prediction of seismic collapse risk of steel moment frame mid-rise structures by meta-heuristic algorithms. Earthq Eng Eng Vib 2016;15(4):743–57. https://doi.org/10.1007/s11803-016-0362-9.

[19] Burton HV, Sreekumar S, Sharma M, Sun H. Estimating aftershock collapse vulnerability using mainshock intensity, structural response and physical damage indicators. Struct Saf 2017;68:85–96. https://doi.org/10.1016/j.strusafe.2017.05.009.

[20] Zhang Y, Burton HV, Sun H, Shokrabadi M. A machine learning framework for assessing post-earthquake structural safety. Struct Saf 2018;72:1–6. https://doi.org/10.1016/j.strusafe.2017.12.001.

[21] Kiani J, Camp C, Pezeshk S. On the application of machine learning techniques to derive seismic fragility curves. Comput Struct 2019;218:108–22. https://doi.org/10.1016/j.compstruc.2019.03.004.

[22] Noh NM, Liberatore L, Mollaioli F, Tesfamariam S. Modelling of masonry infilled RC frames subjected to cyclic loads: State of the art review and modelling with OpenSees. Eng Struct 2017;150:599–621. https://doi.org/10.1016/j.engstruct.2017.07.002.

[23] Di Sarno L, Wu JR. Seismic assessment of existing steel frames with masonry infills. J Constr Steel Res 2020;169:106040. https://doi.org/10.1016/j.jcsr.2020.106040.

[24] Di Sarno L, Freddi F, D'Aniello M, Kwon OS, Wu J-R, Gutiérrez-Urzúa F, et al. Assessment of existing steel frames: Numerical study, pseudo-dynamic testing and influence of masonry infills. J Constr Steel Res 2021;185:106873. https://doi.org/10.1016/j.jcsr.2021.106873.

[25] Asteris PG. Lateral stiffness of brick masonry infilled plane frames. J Struct Eng 2003;129(8):1071–9. https://doi.org/10.1061/(ASCE)0733-9445(2003)129:8(1071).

[26] Asteris PG, Antoniou ST, Sophianopoulos DS, Chrysostomou CZ. Mathematical macromodeling of infilled frames: state of the art. J Struct Eng 2011;137(12):1508–17. https://doi.org/10.1061/(ASCE)ST.1943-541X.0000384.

[27] Yekrangnia M, Asteris PG. Multi-strut macro-model for masonry infilled frames with openings. Journal of Building Engineering 2020;32:101683. https://doi.org/10.1016/j.jobe.2020.101683.

[28] Fardis MN, Panagiotakos TB. Seismic design and response of bare and masonry-infilled reinforced concrete buildings part II: infilled structures. J Earthq Eng 1997;1(03):475–503.

[29] Dolšek M, Fajfar P. The effect of masonry infills on the seismic response of a four-storey reinforced concrete frame-a deterministic assessment. Eng Struct 2008;30(7):1991–2001.

[30] Liberatore L, Decanini LD. Effect of infills on the seismic response of high-rise RC buildings designed as bare according to Eurocode 8. Ingegneria sismica 2011;3:7–23.

[31] Nocedal J, Wright SJ. Numerical Optimization. New York: Springer; 2006.

[32] Gupta A, Krawinkler H. Behavior of ductile SMRFs at various seismic hazard levels. J Struct Eng 2000;126(1):98–107. https://doi.org/10.1061/(ASCE)0733-9445(2000)126:1(98).
[33] Gutierrez-Urzua F, Freddi F, Di Sarno L. Comparative analysis of code-based approaches for seismic assessment of existing steel moment resisting frames. J Constr Steel Res 2021;181:106589. https://doi.org/10.1016/j.jcsr.2021.106589.
[34] McKenna F, Fenves GL, Scott MH. Open System for Earthquake Engineering Simulation. Berkeley: University of California; 2000.
[35] Thaler D, Stoffel M, Markert B, Bamer F. Machine-learning-enhanced tail end prediction of structural response statistics in earthquake engineering. Earthq Eng Struct Dyn 2021;50(8):2098–114. https://doi.org/10.1002/eqe.3432.
[36] Federal Emergency Management Agency. FEMA P695. Quantification of Building Seismic Performance. Applied Technology Council: Redwood City, California; 2009.
[37] Pacific Earthquake Engineering Research Center. PEER NGA-West2 Database. Berkeley: University of California; 2013.
[38] Agency FEM. FEMA 365. Prestandard and commentary for the seismic rehabilitation of buildings. Reston, Virginia: American Society of Civil Engineers:; 2000.